

Material dispersion by oceanic internal waves

Peng Wang¹  · Tamay M. Özgökmen¹ · Angelique C. Haza¹

Received: 5 May 2016 / Accepted: 9 November 2016
© Springer Science+Business Media Dordrecht 2016

Abstract Internal gravity waves that are generated in the open ocean have a universal frequency spectrum, called Garrett–Munk spectrum. By initializing internal waves that satisfy the Garrett–Munk spectrum in a non-hydrostatic numerical model, we investigate the material dispersion produced by these internal waves. Three numerical experiments are designed: Exp.-1 uses a linearly stratified fluid, Exp.-2 has an upper mixed layer, and Exp.-3 incorporates a circular front into the upper mixed layer. Resorting to neutrally buoyant particles, we investigate the dispersion in terms of metrics of the relative dispersion and finite-scale Lyapunov exponent (FSLE). Exp.-1 shows that the dispersion regime produced by these internal waves is between ballistic and diffusive based on relative dispersion, and is however ballistic according to FSLE. The maximum FSLE at scales of 100 m is about 5 day⁻¹, which is comparable to that calculated using ocean drifters. Exp.-2 demonstrates that internal waves can generate flows and material dispersion in an upper mixed layer. However, when mixed layer eddies are present, as in Exp.-3, the dispersion in the mixed layer is controlled by the eddies. In addition, we show that inertial oscillations do not affect the relative dispersion, but impact FSLE at scales of inertial oscillations.

Keywords Relative dispersion · Finite-scale Lyapunov exponent (FSLE) · Garrett–Munk spectrum · Inertial oscillation

1 Introduction

Forecasts of material dispersion in the ocean, such as the dispersion of salinity, heat, dissolved gases, nutrients and pollutants, are important for the ocean ecosystem, economy and human society. A natural way to study the material dispersion is the Lagrangian method, which involves the solutions of the following equation:

✉ Peng Wang
pwang@rsmas.miami.edu

¹ Rosenstiel School of Marine and Atmospheric Science, University of Miami, Miami, FL 33149, USA

$$\frac{d\mathbf{r}}{dt} = \mathbf{v}(t) = \mathbf{u}(\mathbf{x}, t), \tag{1}$$

where \mathbf{r} is the particle position vector, $\mathbf{v}(t)$ is the Lagrangian velocity along a particle’s trajectory, and $\mathbf{u}(\mathbf{x}, t)$ is the Eulerian velocity.

The Lagrangian metrics of dispersion can be divided into two categories, i.e., single-particle statistics and multiple-particle (pairs or groups) statistics [19]. In this study, we focus on the pairwise statistics, particularly on the metrics of relative dispersion and finite-scale Lyapunov exponent (FSLE).

The relative dispersion is defined as

$$D^2(t) = \langle (\mathbf{r}_2(t) - \mathbf{r}_1(t))^2 \rangle, \tag{2}$$

where \mathbf{r}_1 and \mathbf{r}_2 are the position vectors of two particles, and where $\langle \cdot \rangle$ indicates averaging over all particle pairs. The concept of relative dispersion was initiated by Richardson [32], who was trying to explain the increase of relative diffusivity ($\frac{1}{2} \frac{dD^2}{dt}$) in the atmosphere. Richardson found that the relative diffusivity is scale-dependent, proportional to $D^{4/3}$, and that the relative dispersion obeys the power law of $D^2 \propto t^3$. The relative dispersion is computed by averaging the separation distances between particles at fixed times; consequently, the relative dispersion mixes the separations at various spatial scales, and thereby is affected by the outliers of separation distances.

To address material dispersion at specific spatial scales, the scale-dependent Lyapunov exponent is proposed [1, 2], called the finite-scale Lyapunov exponent (FSLE), with the definition of

$$\lambda(\delta) = \frac{\ln(\alpha)}{\langle \tau(\delta) \rangle}, \tag{3}$$

where $\langle \tau(\delta) \rangle$ is the time required for two particles to separate from a distance of δ to $\alpha\delta$, and where $\langle \cdot \rangle$ means averaging over all particle pairs; the factor α is typically in the range of $1 < \alpha < 2$ [15]. FSLE is calculated by averaging the separation times (τ) at given distances (δ), and thus measures dispersion at specific spatial scales (δ).

Four common dispersion regimes (Table 1) are defined based on relative dispersion and FSLE [8, 19]. In view of dimensional analysis, if the relative dispersion scales as $D^2 \propto t^\alpha$, then the FSLE scales as $\lambda \propto \delta^{-2/\alpha}$ [19].

Dispersion regimes depend on the underlying flows; a relation between the dispersion regime and flow’s kinetic energy wavenumber spectrum, $E(k) \propto k^{-\beta}$, has been established (e.g., [3–5]). In terms of the spectrum’s slope ($-\beta$), two general dispersion regimes are defined, namely the local regime and nonlocal regime [5]. In a local regime, the dispersion of particles is dominated by flows with scales comparable to the separation distances between particles; while in a nonlocal regime, the dispersion is controlled by flows with

Table 1 Common dispersion regimes defined by relative dispersion and FSLE

Dispersion regime	Relative dispersion $D^2(t)$	FSLE $\lambda(\delta)$
Exponential	$D^2 \propto e^{\lambda t}$	$\lambda = \text{const.}$
Richardson	$D^2 \propto t^3$	$\lambda \propto \delta^{-2/3}$
Ballistic	$D^2 \propto t^2$	$\lambda \propto \delta^{-1}$
Diffusive	$D^2 \propto t$	$\lambda \propto \delta^{-2}$

scales much larger than the separation distances. If the slope is $1 < \beta < 3$ (shallow spectrum), the dispersion is local, and obeys $D^2 \propto t^{4/(3-\beta)}$ or $\lambda \propto \delta^{(\beta-3)/2}$ [35]; if the slope is $\beta \geq 3$ (steep spectrum), the dispersion is nonlocal, and follows $D^2 \propto e^{\lambda t}$ or $\lambda = \text{const}$. For example, with a shallow spectrum $E(k) \propto k^{-5/3}$, the relative dispersion is in local regime and scales as $D^2 \propto t^3$, which is the Richardson regime. With a steep spectrum $E(k) \propto k^{-3}$, the relative dispersion is nonlocal, and obeys $D^2 \propto e^{\lambda t}$, which is the exponential regime.

On the other hand, knowing the dispersion regimes produced by a flow, we can infer the flow's kinetic energy spectrum, $E(k) \propto k^{-\beta}$. For instance, a local dispersion regime (e.g., Richardson regime) implies a shallow kinetic energy spectrum ($1 < \beta < 3$); while a nonlocal dispersion regime (e.g., exponential regime) indicates a steep kinetic energy spectrum ($\beta \geq 3$). Besides, the diffusive and ballistic regimes may correspond to an energy spectrum with $\beta \leq 1$ at large spatial scales. When the separation distance between particles is large enough that the Lagrangian velocities of particles become uncorrelated, the dispersion regime is diffusive, and further is ballistic if a shear persists in the background flow [16, 19].

Whether or not the sub-mesoscale flows are important for material transport can be determined by the dispersion regime at sub-mesoscales [26, 35]. If the dispersion regime at sub-mesoscales is nonlocal, the material dispersion at sub-mesoscale is controlled by mesoscale flows; thus, the ocean models and satellite altimeters that can resolve the mesoscales are sufficient to predict the dispersion, without the need of capturing the sub-mesoscales. However, if the dispersion regime at sub-mesoscales is local, the material dispersion at sub-mesoscales is controlled by the sub-mesoscale flows; hence, to accurately predict the material dispersion, ocean models and satellite altimeters have to resolve the sub-mesoscales.

Material dispersion has been widely investigated using drifters and floats in different oceans, such as the North Pacific [10, 17], the Atlantic [7, 20, 22], the Southern Ocean [37, 38], the Gulf of Mexico [21, 28], the Mediterranean Sea [14, 29, 30, 34, 35], and the Nordic Sea [18], as well as using numerical simulations (e.g., [15, 23, 24, 26, 41]). These dispersion studies are conducted in ocean currents, various-scale eddies, Langmuir circulations, thermal convections, etc. However, the dispersion by pure oceanic internal waves, to our knowledge, has not been investigated, and is the purpose of our study.

The oceanic internal waves in this study are inertia-internal gravity waves that have frequencies bounded by the local inertial frequency and buoyancy frequency. Internal waves observed in the open ocean have a universal spectrum, namely the Garrett–Munk frequency spectrum [12]. These internal waves have a horizontal wavelength of several kilometers, wave amplitude of tens of meters, and wave period from tens of minutes to hours (e.g., [13, 25]). However, internal waves that satisfy the Garrett–Munk spectrum are difficult to occur in ocean models. We are not aware of any models that spontaneously generate internal waves satisfying the Garrett–Munk spectrum; thus, we need to initialize the oceanic internal waves that satisfy the Garrett–Munk spectrum. Once initialized, the internal waves evolve without any wave sources; meanwhile, particles are released into the internal waves for dispersion measurement. This study represents a scenario that internal waves with Garrett–Munk spectrum propagate from an open ocean into a region away from any wave sources, and gradually decay in this region. With these internal waves we explore whether or not internal waves can produce material dispersion, and whether the internal waves can cause material dispersion within an upper mixed layer. Also, the dispersion under both internal waves and mixed layer eddies is investigated.

2 Method

2.1 Numerical model

Our numerical experiments are conducted with NEK5000, which solves Navier–Stokes equations using the spectral element method (e.g., [11, 27]). NEK5000 has the high-order accuracy and geometry flexibility, and has been used to study geophysical fluid dynamics, including submesoscale instabilities (e.g., [26]), chaotic advection inside an ocean eddy [31, 33], hydrodynamic instabilities of a geophysical vortex [39] and spiral inertial waves [40].

NEK5000 integrates the dimensionless Boussinesq equations:

$$\frac{\partial \mathbf{u}}{\partial t} + (\mathbf{u} \cdot \nabla) \mathbf{u} = -\nabla p - \frac{1}{Ro} \hat{\mathbf{z}} \times \mathbf{u} - \frac{1}{Fr^2} \rho' \hat{\mathbf{z}} + \frac{1}{Re} \nabla^2 \mathbf{u}, \tag{4a}$$

$$\nabla \cdot \mathbf{u} = 0, \tag{4b}$$

$$\frac{\partial \rho'}{\partial t} + (\mathbf{u} \cdot \nabla) \rho' = \frac{1}{Pe} \nabla^2 \rho'. \tag{4c}$$

The Rossby number is given by $Ro = U/(fL)$, where U and L are the typical horizontal velocity and horizontal wavelength of internal waves. $f = 2\Omega$ is the Coriolis parameter, with Ω being the angular velocity of the background rotation. The Froude number is defined as $Fr = U/NH$, where N is the buoyancy frequency and H is the typical vertical wavelength. The Reynolds number is given by $Re = UL/\nu$, where ν is the kinematic viscosity. $Pe = UL/\kappa$ is the Péclet number and κ is the diffusivity of density. $\mathbf{u} = (u, v, w)$ is the velocity in the x, y, z directions, p is the dynamic pressure, and ρ' is the density anomaly. $\hat{\mathbf{z}}$ is the unit vector in the vertical direction, and operator $\nabla = (\frac{\partial}{\partial x}, \frac{\partial}{\partial y}, \frac{\partial}{\partial z})$.

In addition to Eq. (4), NEK5000 integrates the advection-diffusion Eq. (5) for the passive tracer:

$$\frac{\partial C}{\partial t} + (\mathbf{u} \cdot \nabla) C = \frac{1}{Pe} \nabla^2 C, \tag{5}$$

and the Lagrangian advection Eq. (6) for passive, neutrally-buoyant particles:

$$\frac{d\mathbf{x}}{dt} = \mathbf{u}, \tag{6}$$

where \mathbf{x} is the particle position.

The numerical domain (Fig. 1) is a cylinder with diameter $D_c = 52$ km and height $H_c = 2.6$ km; the domain size is large enough to contain internal waves of various scales. The domain is discretized into $K = 2560$ quadrilateral elements; on each element, the solutions are approximated by Legendre polynomials with order $N_p = 17$, which generates about $K(N_p + 1)^3 = 14,929,920$ grid points. The grid spacing is uneven, ranging from 0.39 to 459 m. The boundary conditions are free-slip on the top and bottom, and no-slip on the sidewall; no flux is across boundaries. The numerical computation is performed with 168 processors of a recent computer cluster; a typical simulation costs about 3 weeks.

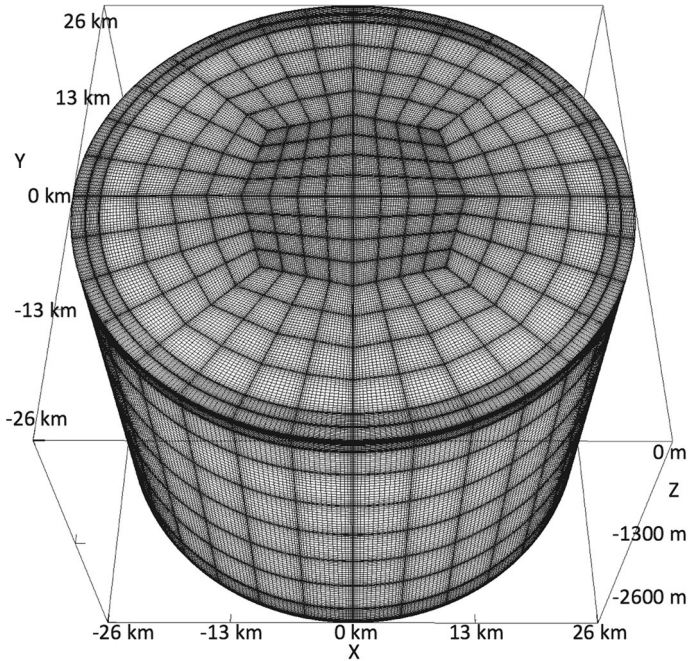


Fig. 1 The numerical domain with 2560 quadrilateral elements (vertically stretched image)

2.2 Initialization of Garrett–Munk internal waves

The Garrett–Munk spectrum is given by Munk [25]

$$E(\omega, j) = \frac{2b^2 f N_0 N E_{GM}}{\pi} \frac{\omega^2 + f^2}{\omega^3 \sqrt{\omega^2 - f^2}} \frac{(j^2 + j_*^2)^{-1}}{\sum_{j=1}^{\infty} (j^2 + j_*^2)^{-1}}, \tag{7}$$

where ω is the internal wave frequency and j is the vertical mode number; other parameters are listed in Table 2.

The method of initializing Garrett–Munk internal waves is proposed by Sun and Kunze [36]; its procedure is as follows: Treat the spectrum in Eq. (7) as a probability density function, and then use the Monte-Carlo method to find random sampling schemes for internal wave frequency ω , vertical mode number j , and wave amplitude. For example, a random sampling scheme for frequency ω can be constructed using the term of $(\omega^2 + f^2)/(\omega^3 \sqrt{\omega^2 - f^2})$ in Eq. (7); that is

$$\frac{\omega^2 + f^2}{\omega^3 \sqrt{\omega^2 - f^2}} = \left(1 + \frac{f^2}{\omega^2}\right) \frac{1}{\omega \sqrt{\omega^2 - f^2}}. \tag{8}$$

Integrate and normalize the term of $\frac{1}{\omega \sqrt{\omega^2 - f^2}}$ in Eq. (8), yielding

Table 2 Parameters used in the Garrett–Munk spectrum

$f = 7.3 \times 10^{-5} \text{ rad s}^{-1}$	Coriolis frequency at 30° N
$N_0 = 50f = 3.7 \times 10^{-3} \text{ rad s}^{-1}$	Reference buoyancy frequency
$N(z) = N_0 e^{z/b}$	Depth-dependent buoyancy frequency
$b = 1300 \text{ m}$	Stratification depth scale
$E_{GM} = 6.3 \times 10^{-5}$	Dimensionless spectral energy level
$j_* = 3$	Peak vertical mode number
$K_{zc} = \frac{1}{3Ri_c j_* b E_{GM}}$	Cutoff vertical wavenumber
$Ri_c = N^2 / \left(\frac{cu}{\overline{cz}} \right)^2 = 2$	Richardson number associated with K_{zc}

$$\frac{\int_f^\omega \frac{1}{\omega \sqrt{\omega^2 - f^2}} d\omega}{\int_f^{N_0} \frac{1}{\omega \sqrt{\omega^2 - f^2}} d\omega} = \frac{\arccos(f/\omega)}{\arccos(f/N_0)} = \text{rand}(e) \text{ ,} \tag{9}$$

where $\text{rand}(e)$ represents a random number in $[0, 1]$. Inverting Eq. (9) for ω , we obtain the random sampling scheme for the wave frequency

$$\omega = \frac{f}{\cos[\arccos(f/N_0)\text{rand}(e)]} \text{ .} \tag{10}$$

Similarly, we can find random sampling schemes for the vertical mode number j , and wave amplitude. Using these sampling schemes, we sample 10,000 wave frequencies ω , vertical mode numbers j , and wave amplitudes (max. velocity of waves = 0.2 m/s). With the wave frequency ω and vertical mode number j , we obtain the vertical wavenumber K_z using the relation of

$$K_z = \frac{\pi j}{b} \sqrt{\frac{N^2 - \omega^2}{N_0^2 - \omega^2}} \text{ .} \tag{11}$$

Then we determine the horizontal wavenumber in terms of the dispersion relation of inertia-inertial gravity waves; the direction of horizontal wave vector $\theta = \arctan(K_y/K_x)$ is randomly chosen from $[0, 2\pi]$ to ensure the horizontal isotropy, where (K_x, K_y) are the horizontal wavenumber in (x, y) direction. Now we have constructed 10,000 waves; then we sum them up to obtain the final internal waves that satisfy the Garrett–Munk spectrum. For more details on initializing Garrett–Munk internal waves, please refer to the work by Sun and Kunze [36].

As shown in Fig. 2, the initialized internal waves have a frequency spectrum with a slope of -2 between $f < \omega < N$, which is consistent with the Garrett–Munk spectrum. Also, the spectrum of initialized internal waves captures other features of the Garrett–Munk spectrum, such as a quick change in the near-inertial frequency ($\omega \sim f$), an energy peak at the inertial frequency f , and an energy cutoff at the buoyancy frequency N [13].

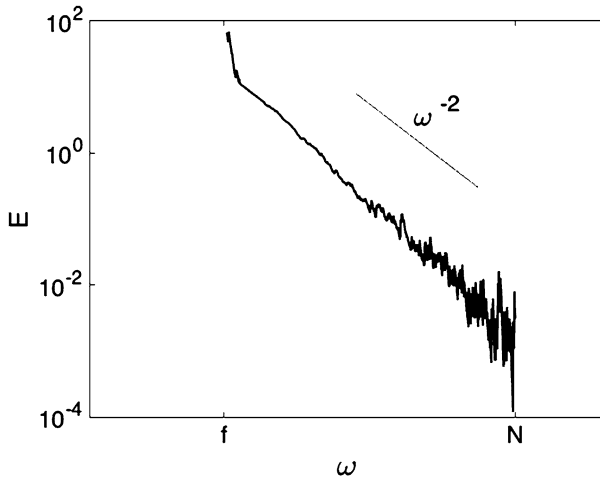


Fig. 2 The frequency spectrum of the initialized internal waves

3 Analysis of material dispersion

3.1 Description of experiments

We design three numerical experiments that are distinguished by the initial density field: Exp.-1 has a linear density stratification (Fig. 3b); Exp.-2 possesses an upper mixed layer of depth of 140 m, and a pycnocline below (Fig. 3c); Exp.-3 incorporates a circular front in the upper mixed layer, which will drive a cyclonic mixed layer eddy. Exp.-1 investigates whether or not pure internal waves can produce dispersion. Exp.-2 explores whether the internal waves can cause dispersion inside an upper mixed layer. Exp.-3 examines the dispersion under both internal waves and mixed layer eddies. All three experiments have the same parameters of Rossby number $Ro = 2$, Froude number $Fr = 0.5$, Reynolds number $Re = 10^5$ and Péclet number $Pe = 7 \times 10^5$, and the same initial internal waves; particularly in Exp.-2 and Exp.-3, the mixed layer is initially motionless.

Internal waves are visualized by density isosurfaces shown in Fig. 4. The vertical oscillation of density isosurface at the mid-depth has a similar amplitude in all three experiments; however, the oscillation in the pycnocline of Exp.-2 and 3 is weaker than that in the sub-surface of Exp.-1. The weaker oscillation is due to the larger density gradient in the pycnocline, the buoyancy frequency of which is about twice of that in the sub-surface of Exp.-1 according to Fig. 3a; a larger density gradient suppresses the vertical motions more, leading to weaker oscillations.

Material dispersion by internal waves is investigated based on two metrics, which are the relative dispersion and FSLE. We release particles at three depths: $D1 = 65$ m inside the mixed layer, $D2 = 208$ m inside the pycnocline layer, and $D3 = 1300$ m at the mid-depth (Fig. 5a); in Exp.-1, depths $D1$ and $D2$ represent the sub-surface and upper layer, for Exp.-1 does not have a mixed layer and pycnocline. At each depth, particles are divided into five groups (Fig. 5b), and are released at five different places; particularly in Exp.-3, the central particle group A released in the mixed layer is right

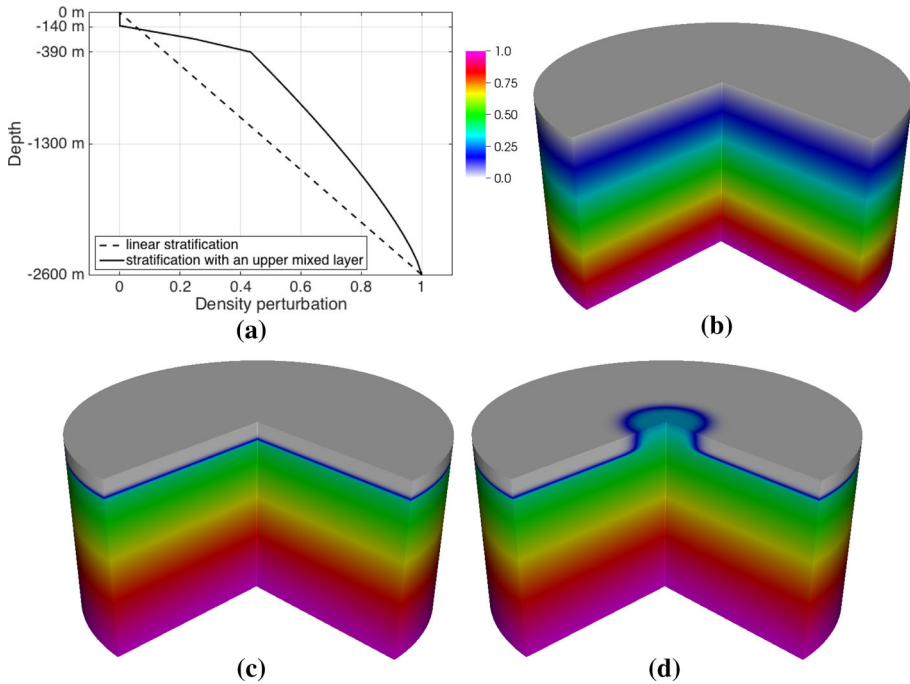


Fig. 3 **a** Vertical profiles of the initial density field in Exp.-1 and Exp.-2. The 3D distribution of initial density field in **b** Exp.-1 with a linear stratification, **c** Exp.-2 with an upper mixed layer, and **d** Exp.-3 with a circular front inside the upper mixed layer

inside the circular front (*cf.* Fig. 3d). The initial separation distance between two particles is 117 m.

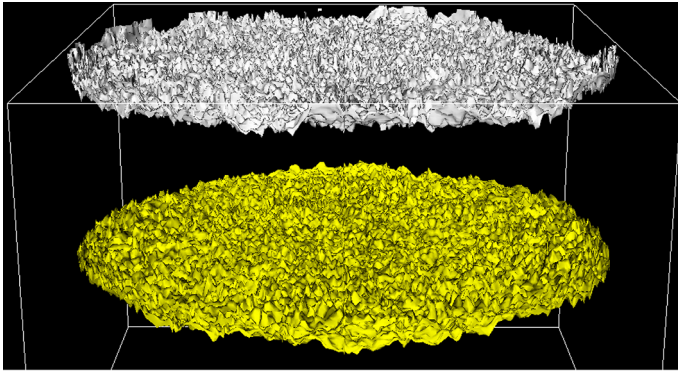
3.2 Exp.-1: linear density stratification

Particles are advected by the 3D velocity of internal waves with a time step of 2 s; the advection terminates before particles reach the domain boundary (Fig. 6).

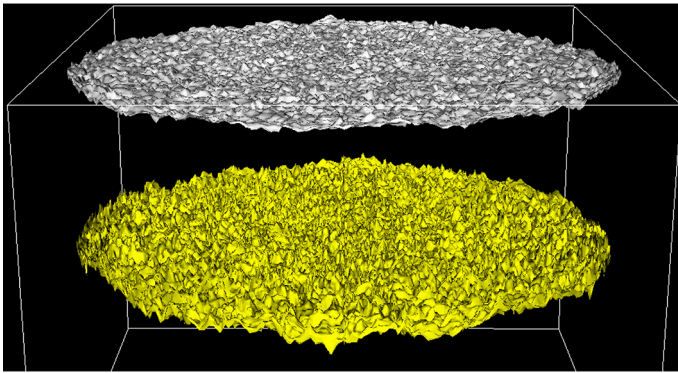
3.2.1 Relative dispersion analysis

At the mid-depth, the relative dispersion computed from each particle group is almost the same to each other (Fig. 7a); at other two depths, the relative dispersion from each group also nearly coincides with each other. The nearly same characteristics of relative dispersion implies that the dispersion in Exp.-1 does not depend on where particles are released. In addition, the mesh grid spacing (resolution) varies with particle groups, but the relative dispersion of all groups is nearly the same, implying the current spatial resolution do not affect the dispersion.

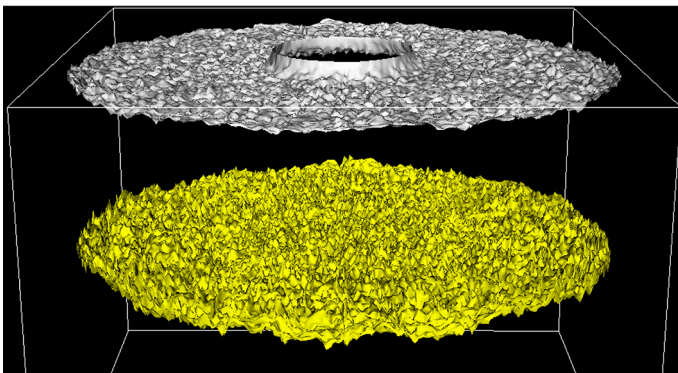
The average relative dispersion shown in Fig. 7a well represents the dispersion of every particle group; thus, we adopt the average relative dispersion in analyzing Exp.-1.



(a)



(b)



(c)

Fig. 4 Density isosurface in **a** Exp.-1, **b** Exp.-2 and **c** Exp.-3 after one day. In each figure, the lower surface locates at the mid-depth; the upper one is inside the sub-surface (Exp.-1) or the pycnocline (Exps.-2, 3)

According to Fig. 7b, c, the average relative dispersion at three depths behaves similar: before 0.1 days, it grows exponentially in time, i.e., $D^2 \propto e^{12t}$ (cf. Fig. 7b); then, it transits to a regime scaling as $D^2 \propto t^{1.5}$ (cf. Fig. 7c), which is between the ballistic and diffusive

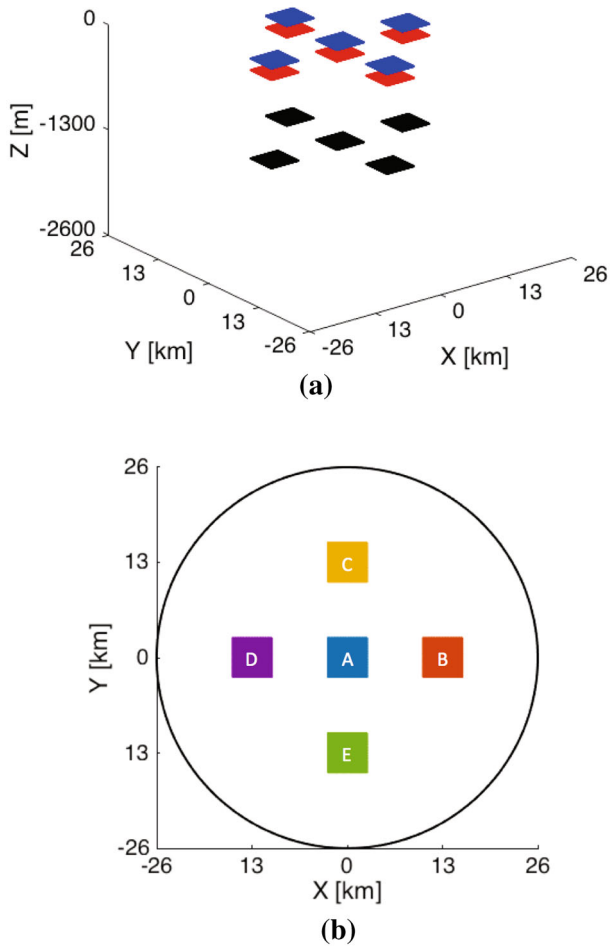


Fig. 5 **a** Particles released at three depths. **b** Five particle groups distributed at each depth; the *circle* represents the domain boundary

regime; about one day later, the relative dispersion still increases but exhibits oscillations; after 5 days, the relative dispersion again scales as $D^2 \propto t^{1.5}$.

3.2.2 FSLE analysis

The FSLE calculated from each particle group is similar to each other (Fig. 8a), and so is the average FSLE (Fig. 8b). As indicated by FSLE, the dispersion regime is ballistic ($\lambda \propto \delta^{-1}$) at spatial scales smaller than ~ 1000 m and larger than ~ 3000 m; between the two scales, the dispersion regime ($\lambda \propto \delta^{-1.5}$) is between ballistic and diffusive.

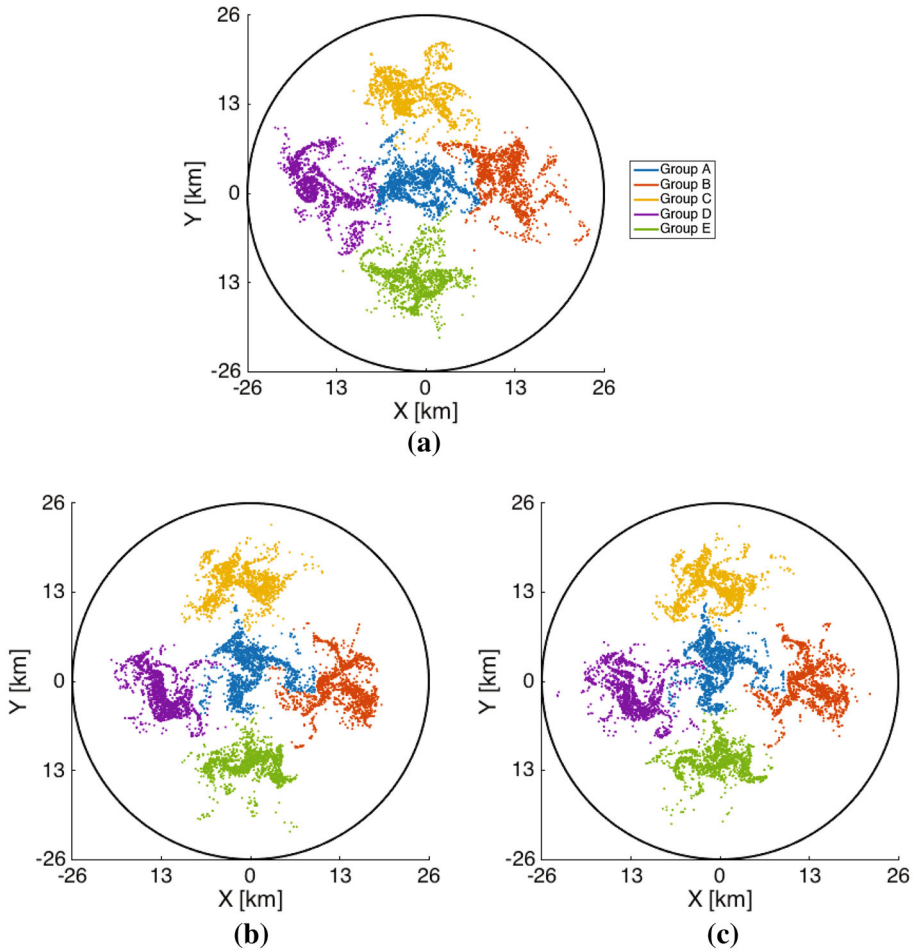


Fig. 6 Exp.-1: Positions of particles at 28.3 days after the release at **a** mid-depth (1300 m), **b** upper layer (208 m) and **c** sub-surface (65 m) in a 2D view

3.3 Exp.-2: upper mixed layer

In Exp.-2, the upper mixed layer (*cf.* Fig. 3c) is initially motionless; internal waves are initialized below the mixed layer. As internal waves continuously hit the base of the mixed layer, weak flows are generated within the mixed layer.

As shown in Fig. 9, the dispersion of particles changes with depth. At the mid-depth, particles have the largest dispersion (Fig. 9a); at the pycnocline (Fig. 9b) and mixed layer (Fig. 9c), each particle group remains compact, dispersing much less than the groups at mid-depth.

3.3.1 Relative dispersion analysis

At each depth, the relative dispersion calculated from each particle group is almost identical to each other; thus, the average relative dispersion is used for analysis. As shown

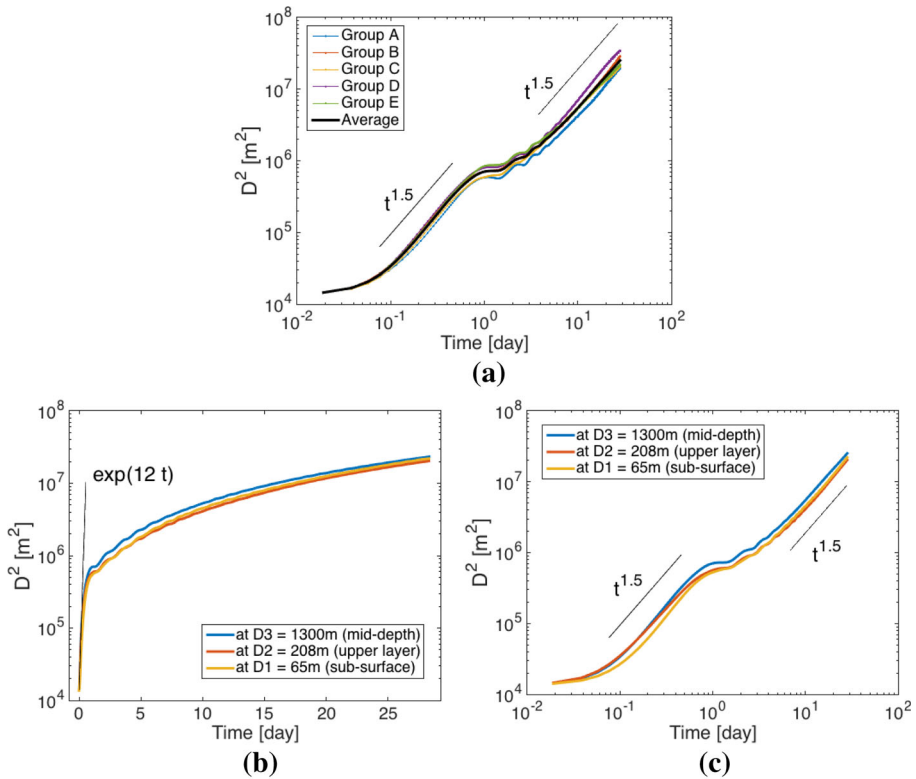


Fig. 7 Exp.-1: **a** Relative dispersion calculated from each particle group released at the mid-depth; the *thick black curve* represents the relative dispersion averaged over all particle groups released at the mid-depth. Average relative dispersion at three depths in **b** semi-log frame and **c** log–log frame. [The exponential fit and power law are also displayed; the unit of growth rate of D^2 is (day^{-1})]

in Fig. 10, the average relative dispersion changes with depth, implying that the dispersion in Exp.-2 is depth-dependent.

At the mid-depth, the relative dispersion is exponential ($D^2 \propto e^{12t}$) when time is less than 0.1 days (Fig. 10a); then the dispersion transits to the regime of $D^2 \propto t^{1.5}$; about 1 day later, the relative dispersion shows oscillations; after 5 days, the relative dispersion scales as $D^2 \propto t^{1.4}$ that is a regime between ballistic and diffusive.

At the pycnocline, the relative dispersion grows exponentially ($D^2 \propto e^{0.3t}$); after 3 days, the relative dispersion gradually transits to a regime of $D^2 \propto t^{1.7}$ (cf. Fig. 10b) that is close to the ballistic regime. At the mixed layer, the relative dispersion is the smallest, and fits an exponential regime of $D^2 \propto e^{0.06t}$ (cf. Fig. 10a), which regime lasts till the end of the experiment.

3.3.2 FSLE analysis

Since at each depth the FSLE calculated from each particle group is nearly the same, the averaged FSLE is used for analysis. According to Fig. 10c, the FSLE curves at three depths span different spatial scales. The FSLE curve at the mid-depth spans the longest, whereas

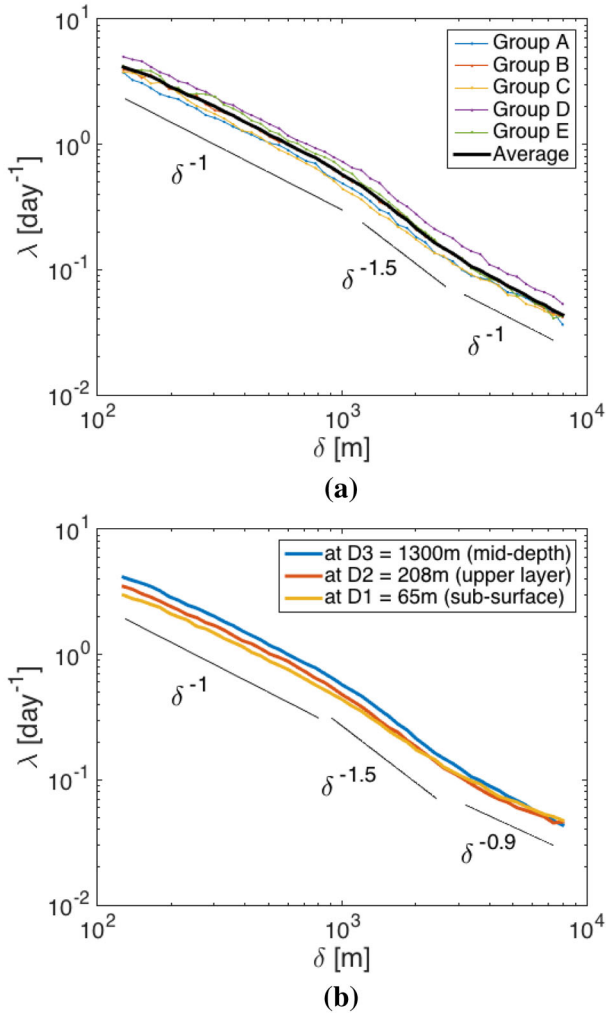


Fig. 8 Exp.-1: **a** FSLE calculated from each particle group released at the mid-depth; **b** FSLE at three depths, averaged over all the particle groups released at the same depth

the curve at the mixed layer spans the shortest. This result is consistent with the relative dispersion shown in Fig. 10a, b. The relative dispersion at the mid-depth is the largest, indicating particles separate to larger distances; thus their FSLE curve spans longer, and has a larger magnitude.

At the mid-depth, the FSLE has a slope of -1 at spatial scales smaller than ~ 1000 m and larger than ~ 3000 m, indicating the ballistic dispersion regime; between the two scales, the FSLE has a slope of -1.5 , meaning a regime between ballistic and diffusive (*cf.* Fig. 10c). At the pycnocline and mixed layer, the magnitude of FSLE is one order of magnitude less than that at the mid-depth. The FSLE at pycnocline has a slope of -0.85 , close to the ballistic dispersion regime.

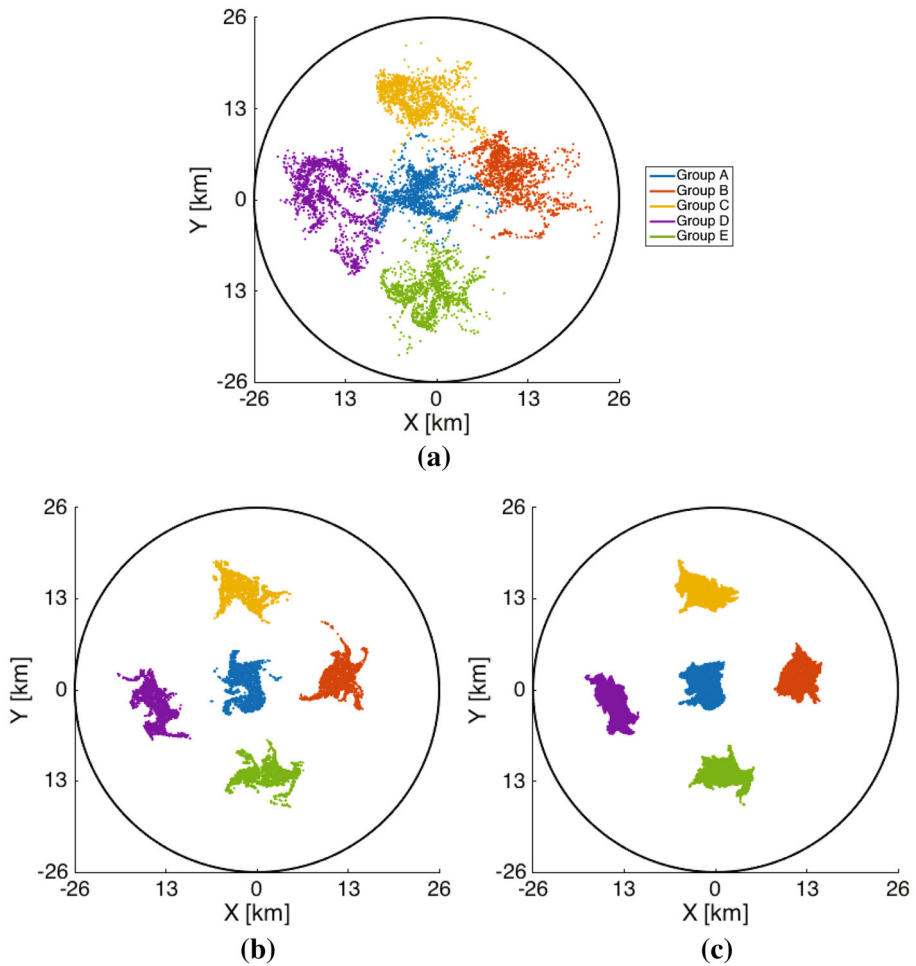


Fig. 9 Exp.-2: Positions of particles at 28.3 days after the release at **a** mid-depth (1300 m), **b** pycnocline (208 m) and **c** mixed layer (65 m) in 2D view

3.4 Exp.-3: upper mixed layer with a circular front

In Exp.-3, a circular front (*cf.* Fig. 3d) in the mixed layer drives a cyclonic eddy with a diameter of about 15 km (Fig. 11a); this eddy later falls apart to smaller eddies due to baroclinic instabilities (Fig. 11c, d). These smaller eddies spread out, changing dispersion nearby them.

Particles released at the pycnocline and mixed layer have very different dispersion. In the mixed layer (Fig. 12c), for example, group A is released right inside the mixed layer eddy (*cf.* Fig. 11a); when this eddy breaks, particles of group A leak out of the eddy and spread widely; some particles are carried away by the reformed eddies to a long excursion. Groups B and C remain compact, whereas groups D and E are stretched into filaments due to the eddies stirring.

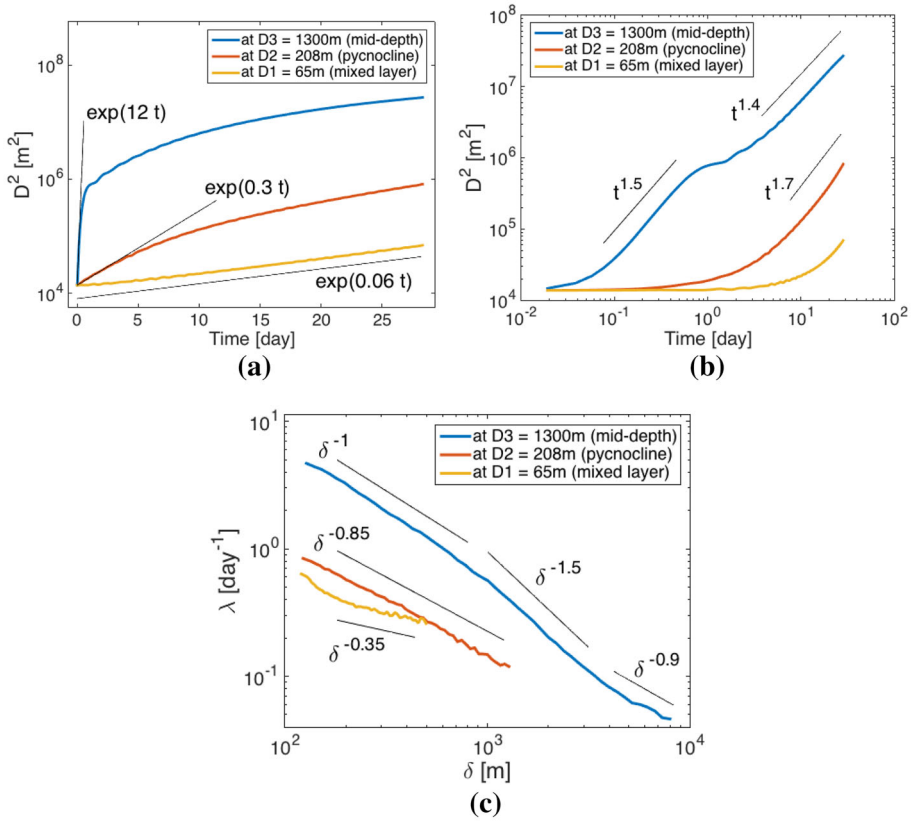


Fig. 10 Exp.-2: Relative dispersion in a **a** semi-log frame and **b** log–log frame; **c** FSLE at three depths. Every curve represents the average over all the particle groups released at the same depth. [The unit of growth rate of D^2 is (day⁻¹).]

3.4.1 Relative dispersion analysis

At the pycnocline (Fig. 13c, d) and mixed layer (Fig. 13e, f), the relative dispersion changes with particle groups due to the biased distribution of mixed layer eddies. The dispersion of particles that are inside or nearby eddies is greatly enhanced. For instance, group A that is released right inside the eddy has the largest dispersion in the mixed layer and pycnocline. Also, the dispersion of groups D and E in the mixed layer suddenly increases around day 13 (*cf.* Fig. 13e, f), as eddies are passing by these groups. However at the mid-depth, all particle groups have an almost identical relative dispersion (Fig. 13a, b), which implies that the mixed layer eddies do not affect the dispersion at the mid-depth in Exp.-3.

Initially, particle groups at all depths have exponential dispersion regimes. Later, the dispersion at mid-depth transits to a regime between ballistic and diffusive. At the pycnocline and mixed layer, the relative dispersion depends on particle groups; for example, at the mixed layer (*cf.* Fig. 13f), the relative dispersion of groups A, D and E belongs to a regime of $D^2 \propto t^{5.2}$, and increases faster than that in Richardson regime, for these groups either are released inside the mixed layer eddy (i.e., group A) or are near the eddies (i.e.,

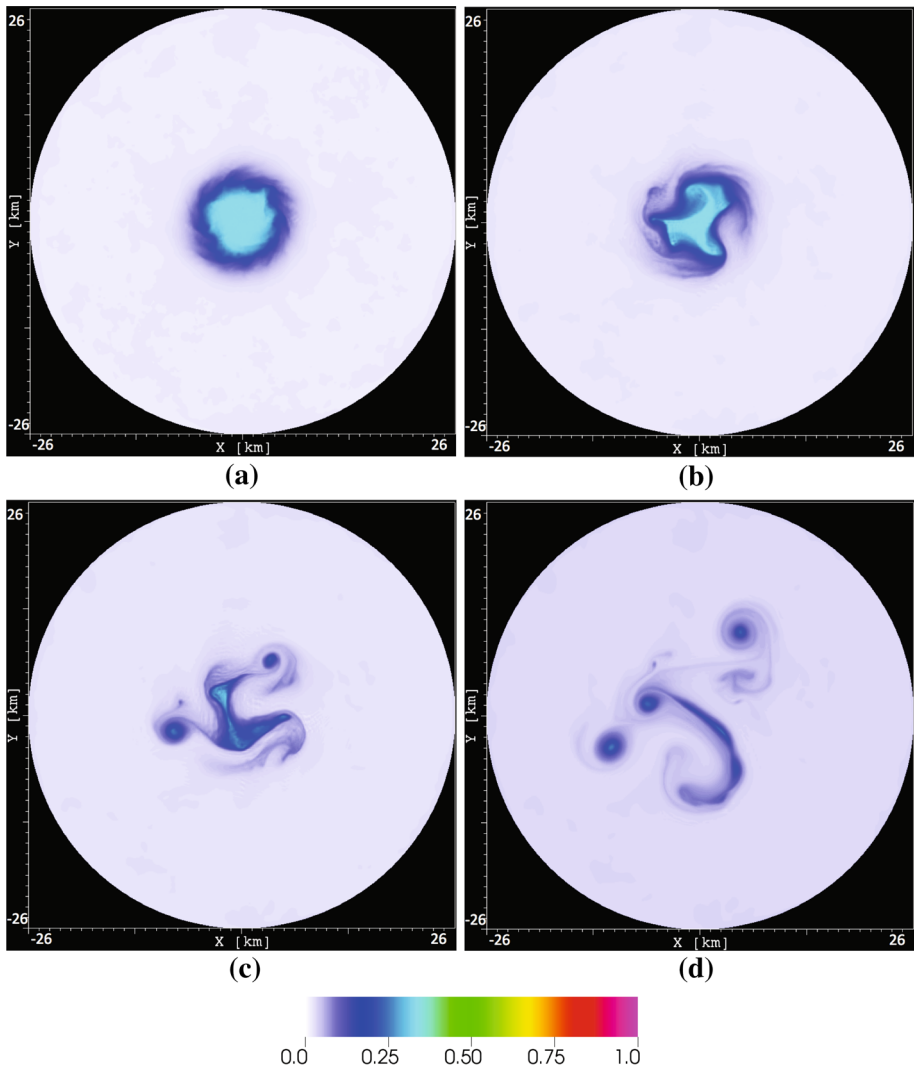


Fig. 11 Exp.-3: Density field on the surface at day **a** 4.2, **b** 8.4, **c** 13.8 and **d** 25.4

groups D and E); nevertheless, the relative dispersion of groups B and C still remains in the exponential regime ($D^2 \propto e^{0.06t}$) with a very small growth rate (*cf.* Fig. 13e), for groups B and C stay away from the eddies.

3.4.2 FSLE analysis

At the mid-depth (Fig. 14a), the FSLE from different particle groups is almost identical, confirming that mixed layer eddies hardly affect the dispersion at the mid-depth in Exp.-3. At spatial scales smaller than ~ 1000 m and larger than ~ 3000 m, the FSLE obeys $\lambda \propto \delta^{-1}$, indicating the ballistic dispersion regime; between the two scales, the FSLE

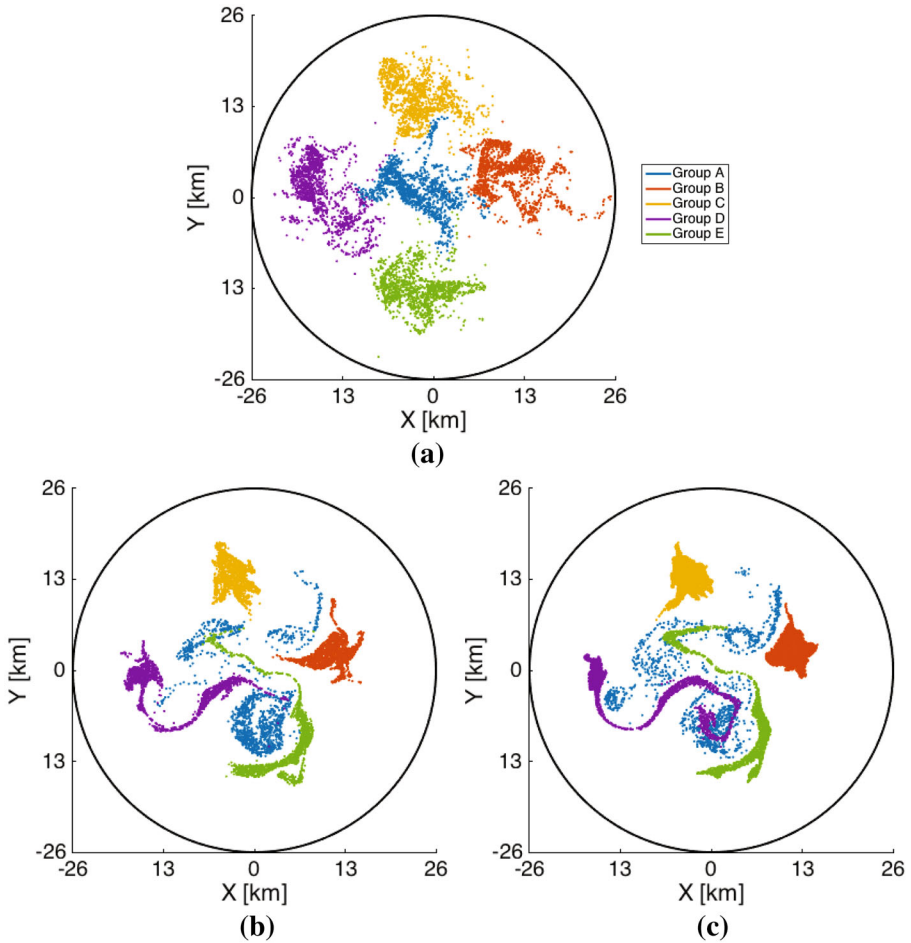


Fig. 12 Exp.-3: Positions of particles after 28.3 days at **a** mid-depth (1300 m), **b** pycnocline (208 m) and **c** mixed layer (65 m) in a 2D view

follows $\delta^{-1.5}$, indicating a regime between ballistic and diffusive.

At the pycnocline and mixed layer (Fig. 14b, c), the FSLE computed from group A stands out from other groups, with a larger magnitude and a wider spatial span. At small spatial scales, the FSLE curves of groups B–E nearly coincide with each other. However at larger scales, the FSLE curves of groups D and E diverge due to the passage of mixed layer eddies.

4 Discussion

In all three experiments, particles released at the mid-depth have similar dispersion: Based on the relative dispersion metric, the dispersion is exponential ($D^2 \propto e^{12t}$) at the beginning; after about 0.1 days, it transits to a regime ($D^2 \propto t^{1.5}$) between ballistic and diffusive; around 5 days, the dispersion resume to the regime of $D^2 \propto t^{1.5}$. In terms of FSLE, at

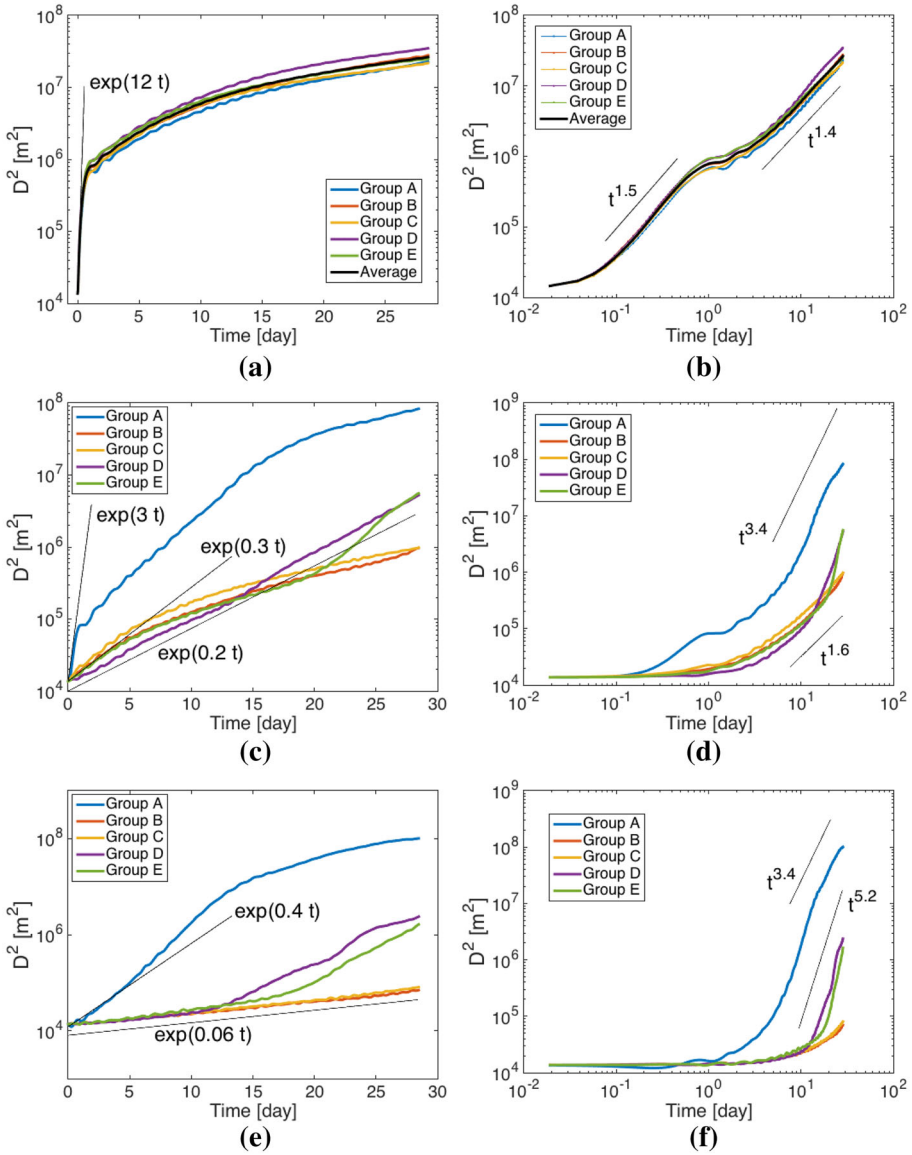


Fig. 13 Exp.-3: Relative dispersion calculated from each particle group released at the **a, b** mid-depth (1300 m), **c, d** pycnocline (208 m) and **e, f** mixed layer (65 m). Left column: semi-log frame; right column: log-log frame. [The unit of growth rate of D^2 is (day^{-1}) .]

spatial scales smaller than ~ 1000 m and larger than ~ 3000 m, the $\lambda \propto \delta^{-1}$ indicates the ballistic dispersion regime, while between the two spatial scales, the $\lambda \propto \delta^{-1.5}$ indicates a regime between ballistic and diffusive.

Exp.-1 has a linear density stratification and a depth-independent buoyancy frequency, which leads to the dispersion being independent on depth (*cf.* Figs. 7c, 8b). By contrast, the buoyancy frequency in Exp.-2 changes with depth, and so does the dispersion (*cf.* Fig. 10).

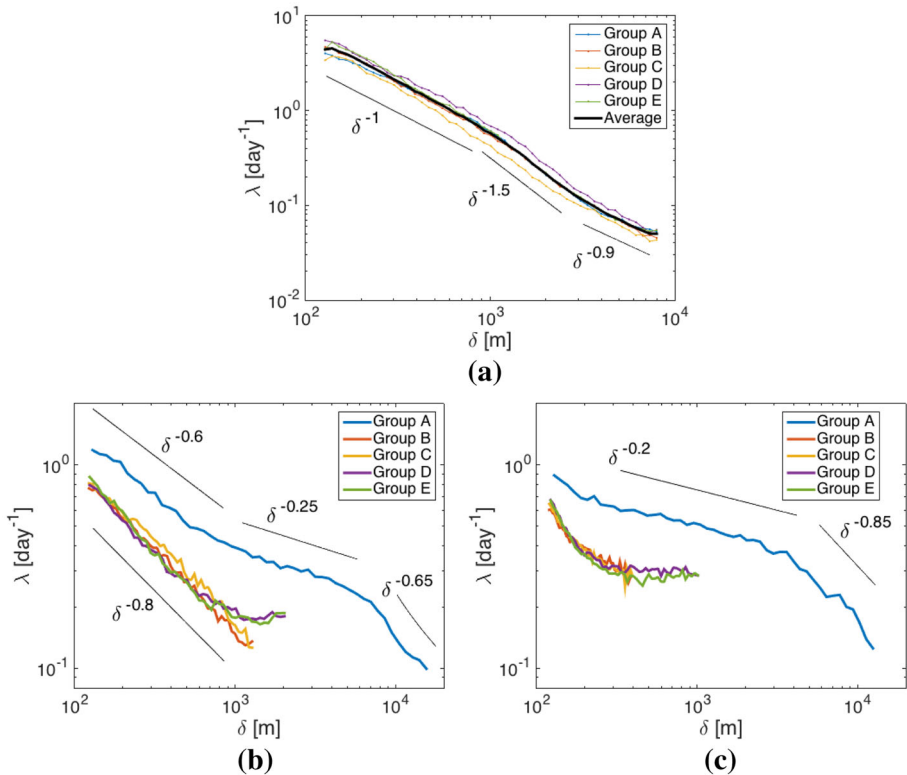


Fig. 14 Exp.-3: FSLE calculated from each particle group released at the **a** mid-depth (1300 m), **b** pycnocline (208 m) and **c** mixed layer (65 m)

The buoyancy frequency in the pycnocline is larger than that at the mid-depth, suppressing flows in the pycnocline and causing smaller dispersion. The above results imply that material dispersion depends on the fluid’s buoyancy frequency.

Internal waves can affect material dispersion in an upper mixed layer. For example, dispersion in the mixed layer of Exp.-2 (*cf.* Fig. 9c) is produced by flows that are generated by the below internal waves; since the generated flow is weak, the associated dispersion is small (*cf.* Fig. 10).

When mixed layer eddies are present, as in Exp.-3, the eddies dominate dispersion in the mixed layer (*cf.* Fig. 13e, f). However, at the mid-depth of Exp.-3, the dispersion is not affected by the mixed layer eddies (*cf.* Figs. 13b, 14a), for these eddies only penetrate to a depth about 800 m, hardly affecting the dispersion at mid-depth (1300 m).

In the long-term dispersion, say 10 days, the relative dispersion produced by internal waves is only a couple of kilometers in our experiments (*cf.* Fig. 7); however, the relative dispersion in the ocean is up to hundreds of kilometers in 10 days, particularly near the surface [28, 35]. Because the ocean contains many processes that contribute to material dispersion, such as wind-driven currents, thermal convections, tidal flows and surface gravity waves; as one of these processes, internal waves contribute significantly to the dispersion only at their own temporal and spatial scales.

In our study, the maximum FSLE at scales of ~ 100 m is about 5 day^{-1} (cf. Fig. 8b), which is comparable to that found in real oceans, such as the Gulf of Mexico [21, 28], the Atlantic Ocean [7], the Mediterranean Sea [14, 34, 35] and Southern Ocean [38]. Therefore, the dispersion by internal waves needs to be counted to predict material dispersion at scales of ~ 100 m in the ocean.

The restoring forces of internal waves in this study are the Coriolis force and buoyancy; therefore, particles trajectories by these internal waves always contains the part from inertial oscillations, which are generated by the Coriolis force. The scale of inertial oscillations is given by V/f , where V is particle speed and f is the local inertial frequency [9]; the inertial oscillation scale in our experiments is less than 1 km. A natural question is: Do inertial oscillations affect the relative dispersion and FSLE? Let's use Exp.-1 to examine this effect. We remove inertial oscillations using a low-pass filter with the cutoff

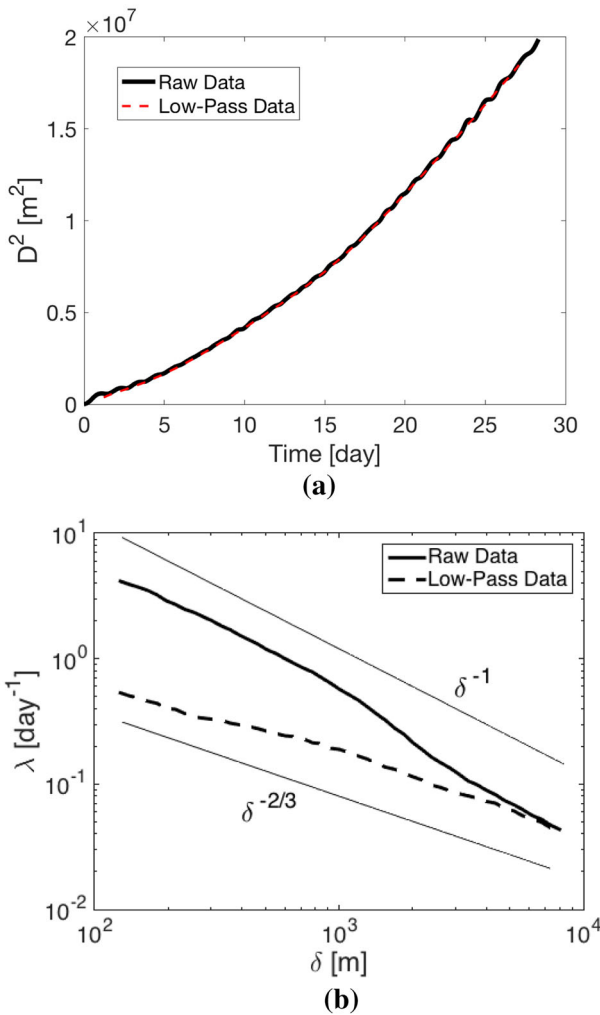


Fig. 15 **a** Relative dispersion **b** FSLE at the mid-depth of Exp.-1. Each curve is the average over five particle groups. Low-pass data removes inertial oscillations

frequency of $(2.5 \text{ days})^{-1}$. After removing inertial oscillations, the relative dispersion remains almost the same (Fig. 15a); however, the FSLE decreases remarkably at scales comparable to that of inertial oscillations (Fig. 15b). Therefore inertial oscillations do not affect the relative dispersion, but impact FSLE at scales of inertial oscillations [6].

Why do inertial oscillations have different effects on the relative dispersion and FSLE? Inertial oscillations create circular particle trajectories; theoretically after an inertial period, particles return to their origins, producing zero relative dispersion. Thus inertial oscillations do not contribute to the relative dispersion. For the FSLE, once two particles are separated to a specific distance by inertial oscillations, the dispersion is counted by FSLE; hence FSLE is subject to inertial oscillations. Nevertheless as shown in Fig. 15b, at larger scales ($>5 \text{ km}$) the FSLE from low-pass data is nearly the same with that from raw data, indicating that inertial oscillations do not affect FSLE at scales larger than that of inertial oscillations. In fact, particle separations by inertial oscillations are around the scales of inertial oscillations; thus at spatial scales much larger than scales of inertial oscillations, the dispersion by inertial oscillations is negligible, and FSLE at these spatial scales becomes robust to inertial oscillations.

When particles do inertial oscillations with different radii, the separation distance between particles may oscillate with time, creating oscillations in relative dispersion (e.g., Fig. 7a). Removing inertial oscillations can remove these dispersion oscillations, smoothing the curve of relative dispersion (Fig. 15a).

Our study confirms that the dispersion regime identified by relative dispersion is not necessarily the same with that identified by FSLE (e.g., [19, 20, 38]). The difference in identifying dispersion regimes is rooted in the definitions of relative dispersion and FSLE: Relative dispersion uses temporal scales to identify regimes, while FSLE uses spatial scales. Due to the distinction in definitions, different dispersion metrics may react distinctly to some dispersion processes, including inertial oscillations. For time-based dispersion metrics (e.g., relative dispersion), inertial oscillations may be not important, but for space-based metrics (e.g., FSLE), inertial oscillations do matter, particularly at scales of inertial oscillations.

5 Conclusion

Using numerical simulations of oceanic internal waves that are initialized with the Garrett–Munk spectrum, we investigate the material dispersion produced by these internal waves. The dispersion is examined by two metrics, the relative dispersion and FSLE. In terms of relative dispersion, the dispersion is exponential at the beginning, and transits to a regime ($D^2 \propto t^{1.5}$) between ballistic and diffusive. In terms of FSLE, the ballistic dispersion regime dominates; the maximum FSLE at scales of 100 m is about 5 day^{-1} , which is comparable to that found by ocean observations. Internal waves can generate flows in an upper mixed layer, leading to material dispersion in the mixed layer; when mixed layer eddies are present, the dispersion is controlled by the eddies. In addition, we show that inertial oscillations do not affect the relative dispersion, but impact FSLE at scales of inertial oscillations.

This study on material dispersion by internal waves is preliminary, due to huge computational challenges of generating internal waves that satisfy the Garrett–Munk spectrum in a numerical model. But it is original since most of the dispersion studies are conducted using models that contain only coherent structures, such as eddies of various sorts.

Acknowledgements We are grateful for the support from the Office of Naval Research (Grant N000141110087) and the BP/The Gulf of Mexico Research Initiative. Also, we thank Dr. Alex Fabregat for helping to process the data input to model, and thank the reviewers for helping to improve our manuscript.

References

1. Artale V, Boffetta G, Celani A, Cencini M, Vulpiani A (1997) Dispersion of passive tracers in closed basins: beyond the diffusion coefficient. *Phys Fluid* 9:3162–3171
2. Aurell E, Boffetta G, Crisanti A, Paladin G, Vulpiani A (1997) Predictability in the large: an extension of the concept of Lyapunov exponent. *J Phys A* 30:1–26
3. Babiano A, Basdevant C, Le Roy P, Sadourny R (1990) Relative dispersion in two-dimensional turbulence. *J Fluid Mech* 214:535–557
4. Batchelor GK (1950) The application of the similarity theory of turbulence to atmospheric diffusion. *Q J R Meteorol Soc* 76:133–146
5. Bennett AF (1984) Relative dispersion: local and nonlocal dynamics. *J Atmos Sci* 41:1881–1886
6. Beron-Vera FJ, LaCasce JH (2016) Statistics of simulated and observed pair separations in the Gulf of Mexico. *J Phys Oceanogr* 46:2183–2199
7. Berti S, Santos FAD, Lacorata G, Vulpiani A (2011) Lagrangian drifter dispersion in the southwestern Atlantic ocean. *J Phys Oceanogr* 41:1659–1672
8. Boffetta G, Celani A, Cencini M, Lacorata G, Vulpiani A (2000) Nonasymptotic properties of transport and mixing. *Chaos* 10:50–60
9. Cushman-Roisin B, Beckers J-M (2011) Introduction to geophysical fluid dynamics, 2nd edn. Academic Press, Cambridge
10. Davis R (1985) Drifter observations of coastal surface currents during CODE: the method and descriptive view. *J Geophys Res* 90:4741–4755
11. Fischer PF (1997) An overlapping Schwarz method for spectral element solution of the incompressible Navier–Stokes equations. *J Comput Phys* 133(1):84–101
12. Garrett C, Munk W (1975) Space-time scales of internal waves: a progress report. *J Geophys Res* 80(3):291–297
13. Garrett C, Munk W (1979) Internal waves in the ocean. *Annu Rev Fluid Mech* 11:339–369
14. Haza AC, Özgökmen TM, Griffa A, Molcard A, Poulain P-M, Peggion G (2010) Transport properties in small-scale coastal flows: relative dispersion from VHF rada measurements in the Gulf of La Spezia. *Ocean Dyn* 60:861–882
15. Haza AC, Poje AC, Özgökmen TM, Martin P (2008) Relative dispersion from a high-resolution coastal model of the Adriatic Sea. *Ocean Model* 22:48–65
16. Iudicone D, Lacorata G, Rupolo V, Santoleri R, Vulpiani A (2002) Sensitivity of numerical tracer trajectories to uncertainties in OGCM velocity fields. *Ocean Model* 4:313–325
17. Kirwan AD, McNally GJ, Reyna E, Merrell WJ (1978) The near-surface circulation of the eastern North Pacific. *J Phys Oceanogr* 8:937–945
18. Koszalka I, LaCasce JH, Orvik KA (2009) Relative dispersion in the Nordic Seas. *J Mar Res* 67:411–433
19. LaCasce JH (2008) Statistics from Lagrangian observations. *Prog Oceanogr* 77:1–29
20. LaCasce JH, Bower A (2000) Relative dispersion in the subsurface North Atlantic. *J Mar Res* 58:863–894
21. LaCasce JH, Ohlmann C (2003) Relative dispersion at the surface of the Gulf of Mexico. *J Mar Res* 61:285–312
22. Lumpkin R, Elipot S (2010) Surface drifter pair spreading in the North Atlantic. *J Geophys Res* 115:C12017
23. Mensa JA, Özgökmen TM, Poje AC, Imberger J (2015) Material transport in a convective surface mixed layer under weak wind forcing. *Ocean Model* 96:226–242
24. Molcard A, Poje AC, Özgökmen TM (2006) Directed drifter launch strategies for Lagrangian data assimilation using hyperbolic trajectories. *Ocean Model* 12:268–289
25. Munk W (1981) Internal waves and small-scale processes. *Evolution of physical oceanography*. MIT Press, Cambridge, pp 264–291
26. Özgökmen TM, Poje AC, Fischer PF, Childs H, Krishnan H, Garth C, Haza AC, Ryan E (2012) On multi-scale dispersion under the influence of surface mixed layer instabilities and deep flows. *Ocean Model* 56:16–30
27. Patera AT (1984) A spectral element method for fluid dynamics: laminar flow in a channel expansion. *J Comput Phys* 54(3):468–488

28. Poje A, Özgökmen TM, Lipphardt BL, Haus BK, Ryan EH, Haza AC, Jacobs GA, Reniers AJHM, Olascoaga MJ, Novelli G, Griffa A, Bero-Vera FJ, Chen SS, Coelho E, Hogan PJ, Kirwan AD, Huntley HS, Mariano AJ (2014) Submesoscale dispersion in the vicinity of the Deepwater Horizon spill. *Proc Natl Acad Sci* 111(35):12693–12698
29. Poulain P-M (1999) Drifter observations of surface circulation in the Adriatic Sea between December 1994 and March 1996. *J Mar Syst* 20:231–253
30. Poulain P-M (2001) Adriatic Sea surface circulation as derived from drifter data between 1990 and 1999. *J Mar Syst* 29:3–32
31. Pratt LJ, Rypina II, Özgökmen TM, Wang P, Childs H, Bebieva Y (2014) Chaotic advection in a steady, three-dimensional, Ekman-driven eddy. *J Fluid Mech* 738:143–183
32. Richardson LF (1926) Atmospheric diffusion shown on a distance-neighbor graph. *Proc R Soc Lond* 110:709–737
33. Rypina II, Pratt LJ, Wang P, Özgökmen TM, Mezic I (2015) Resonance phenomena in a time-dependent, three-dimensional model of an idealized eddy. *Chaos* 25(8):087401
34. Schroeder K, Chiggiato J, Haza AC, Griffa A, Özgökmen TM, Zanasca P, Molcard A, Borghini M, Poulain PM, Gerin R, Zambianchi E, Falco P, Trees C (2012) Targeted Lagrangian sampling of submesoscale dispersion at a coastal frontal zone. *Geophys Res Lett* 39:L11608
35. Schroeder K, Haza AC, Griffa A, Özgökmen TM, Poulain PM, Gerin R, Rixen M (2011) Relative dispersion in the Liguro-Provençal basin: from sub-mesoscale to mesoscale. *Deep Sea Res Part I* 58(3):209–228
36. Sun H, Kunze E (1999) Internal wave-wave interactions. Part I: the role of internal wave vertical divergence. *J Phys Oceanogr* 29(11):2886–2904
37. Trani M, Falco P, Zambianchi E, Sallée JB (2014) Aspects of the Antarctic Circumpolar Current dynamics investigated with drifter data. *Prog Oceanogr* 125:1–15
38. van Sebille E, Waterman S, Barthel A, Lumpkin R, Keating SR, Fogwill C, Turney C (2015) Pairwise surface drifter separation in the western Pacific sector of the Southern Ocean. *J Geophys Res* 120:6769–6781
39. Wang P, Özgökmen TM (2015) How do hydrodynamic instabilities affect 3D transport in geophysical vortices? *Ocean Model* 87:48–66
40. Wang P, Özgökmen TM (2016) Spiral inertial waves emitted from geophysical vortices. *Ocean Model* 99:22–42
41. Zambianchi E, Griffa A (1994) Effects of finite scales of turbulence on dispersion estimates. *J Mar Res* 52:129–148